First-principles study of the conduction mechanism in tantala-based resistive memory devices

Juho Lee, Seunghyun Kim, Hyoseok Kim, Sungduk Hong, Sung Jin Kim and Dae Sin Kim
Computational Science & Engineering
Samsung Electronics
Hwaseong-si, Gyeonggi-do, Korea
Email: juho89.lee@samsung.com

Myung Hun Woo, Joo Heon Kang, Hyun-Mog Park and Daewon Ha
Advanced Device Research, Semiconductor R&D Center
Samsung Electronics
Hwaseong-si, Gyeonggi-do, Korea

***Abstract*—Herein, adopting the Pt/Ta_2O_5/Pt stack, first-principles calculations are carried out to investigate the conduction mechanism of tantala-based resistive switching devices. We first study the formation of conducting filament composed of the TaO_{2-x} from the Ta_2O_5 matrix by modulating the number of oxygen vacancies and find that the TaO_{2-x} filament formation is initiated from the metal contact through the redox reaction. Subsequent current-bias voltage characteristic analyses reveal that the Ta_2O_5 matrix with $\sim 1.4 \times 10^{20}\ cm^{-3}$ oxygen vacancy concentration assumes the low resistance state. It will be emphasized that the conduction mechanism behind the tantala-based resistive switching originates from the carrier concentration variation with the Schottky barrier height modulation according to the oxygen vacancy concentrations. The microscopic understanding accumulated in this study will provide an insight into the development of next-generation tantala-based resistive switching devices.**

***Keywords*—ReRAM, tantala, density functional theory, conducting filament**

I. INTRODUCTION

In recent years, numerous researches on oxide-based resistive switching devices have been reported as a candidate for the next-generation non-volatile memory due to its advantages in scalability and fast switching speed [1-3]. Among the candidates for resistive materials for resistive switching device applications, the tantala-based resistive devices have showed excellent switching performances with high thermal/chemical stability as well as its compatibility with CMOS processes [4, 5]. Interestingly, Ta-O system has only two stable phases of Ta_2O_5 and TaO_2 with a low reaction Gibbs free energy for redox reaction of TaO_x, which is the key to achieve long switching endurance [5]. Previously, through *in situ* scanning transmission electron microscope, the formation of the conductive filamentary TaO_{2-x} channels owing to the migration of oxygen vacancies (V_O) was successfully revealed, thereby understanding the switching mechanism associated with the behavior of V_O as well as its composition modulation [6]. However, the comprehensive interpretation of the high resistance state (HRS) and the low resistance state (LRS) of TaO_{2-x} with the corresponding electrical properties is still lacking, making further systematic improvements difficult.

Here, adopting a first-principles approach that combines density functional theory (DFT) and matrix Green's function (MGF) approaches, we study the electrical and transport properties of the LRS/HRS of Pt(111)/ Ta_2O_{5-x}/Pt(111) heterojunctions. Varying the number of V_O, we first identify the formation of TaO_{2-x} conducting filament (CF) initiated from the metal contact through the redox reaction. We next calculate current-bias voltage (I-V_b) characteristics and find out that the Ta_2O_5 matrix with 9 V_O ($\sim 1.4 \times 10^{20}\ cm^{-3}$) assumes the LRS. Further electronic structure analysis proves that the conduction mechanism of the LRS originates from the combination of the carrier concentration increase and the Schottky barrier height (ϕ_{SBH}) lowering effect due to the TaO_{2-x} CF formation.

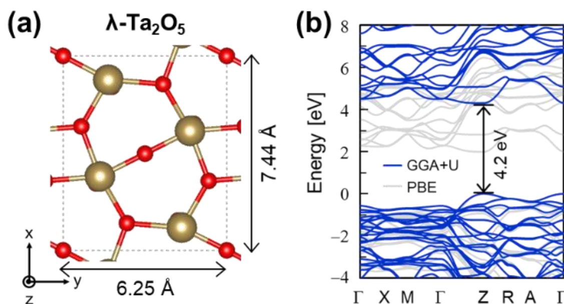

Fig. 1. (a) The atomic structure of λ-Ta_2O_5 and (b) the corresponding electronic band structure.

II. METHOD

A. First-principles Calculations

In modeling the resistive switching device, we adopted a Pt(111)–Ta_2O_5–Pt(111) stack with the Pt–Pt gap distance of 22.8 Å. Here, λ-Ta2O5, which is found to match the experimental results mostly [7], was adopted [Fig. 1(a)]. The simulation cell was a 2×2 Ta_2O_5 supercell with 5×4 Pt(111) to minimize the lattice constant mismatch. DFT calculations were performed using the SIESTA code [8] within the Perdew-Burke-Ernzerhof parameterization of generalized gradient approximation [9]. For the electronic structure and transport calculations, we also adopted GGA+U method for the appropriate description of the exchange and correlation energy of the electrons. On-site Coulomb corrections were applied to both the *d* orbital electrons of tantalum and the *p* orbital electrons of oxygen (U_d = 6 eV and U_p = 9 eV)[10] to reproduce accurate structural parameters and bandgap energies [Fig. 1(b)]. Double ζ-plus-polarization-level numerical atomic orbital basis sets were employed together with the Troullier-Martins type norm-conserving pseudopotentials [11]. The Γ point of Brillouin zone was sampled. The atomic geometries were optimized until the total residual force was below 0.02 eV/ Å using the conjugate gradient algorithm.

XXX-X-XXXX-XXXX-X/XX/$XX.00 ©20XX IEEE

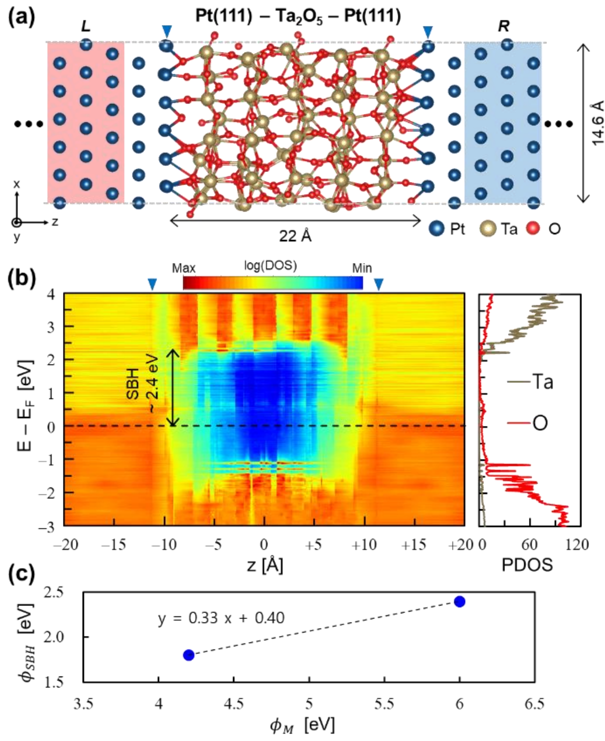

Fig. 2. (a) The atomic structures of Pt(111)/Ta_2O_5/Pt(111) stack. Red and blue boxes indicate *L* and *R* regions, respectively. (b) The corresponding spatially-resolved DOS (*left*) and Ta_2O_5-projected DOS (*right*). The blue downward triangles indicate the position of Pt layer at the metal contact. The black dashed line indicates the Fermi level of the system. (c) The ϕ_{SBH} as function of the ϕ_M. The slope indicates the pinning factor of Ta_2O_5.

B. *Quantum Transport Calculations*

For the quantum transport calculation, we used the DFT-based MGF method implemented within the TranSIESTA code [12]. The surface Green's functions g_s were extracted from separate DFT calculations for three-layer 5 × 4 Pt(111) crystals with the Γ-point sampling along the surface *xy* plane and 10 $k_\perp$-point sampling along the charge-transport *z* direction. The transmission functions were then obtained according to

$$T(E;V_b) = Tr[\Gamma_L(E;V_b)G(E;V_b)\Gamma_R(E;V_b)G^\dagger(E;V_b)] \quad (1)$$

where *G* is the retarded Green's function for the channel, and $\Gamma_{L/R} = i(\Sigma_{L/R} - \Sigma^\dagger_{L/R})$ are the broadening matrices of the left (*L*) and right (*R*) electrodes. The current–bias voltage (*I-V*$_b$) characteristics were calculated by invoking the Landauer-Büttiker formula [13],

$$I(V_b) = \frac{2e}{h}\int_{\mu_L}^{\mu_R} T(E;V_b)[f(E-\mu_R) - f(E-\mu_L)]\,dE. \quad (2)$$

III. Results and Discussions

In Fig. 2(a), we show the atomic structure of the resistive switching device model in which insulating Ta_2O_5 channels are sandwiched between Pt(111) electrodes. The corresponding spatially-resolved density of states (DOS) and the projected DOS of Ta_2O_5 are provided in Fig. 2(b). We initially obtained the band gap of around 3.5 eV in the case of the Ta_2O_5 channel, which is slightly reduced compared to the λ-Ta_2O_5 of 4.2 eV due to the lattice mismatch strain between Ta_2O_5 and Pt. The ϕ_{SBH} of ~2.4 eV at the Pt(111)-Ta_2O_5 interface was obtained [Fig. 2(b), *left*]. We noted that the obtained ϕ_{SBH} is higher than the expected ϕ_{SBH} of 1.15 eV [14] based on the Schottky-Mott rule. In particular, we show the metal induced gap states coupled with O atoms [Fig. 2(b), *right*], and accordingly the Fermi level pinning effect at metal-Ta_2O_5 interfaces is assumed. To clarify its pinning effect, we calculated the pinning factor (*S*) defined as,

$$S = \frac{d\phi_{SBH}}{d\phi_M}, \quad (3)$$

where ϕ_M stands for the metal work function. Here, a Al(111)–Ta_2O_5–Al(111) stack is calculated since Al is a low ϕ_M metal (~4.2 eV) with a lattice constant of 4.05 Å similar to Pt (3.92 Å). As shown in Fig. 2(c), we obtained the ϕ_{SBH} of ~1.8 eV at the Al(111)-Ta_2O_5 interface. Accordingly, the *S* is determined to be 0.33, showing the Fermi level pinning behavior of Ta_2O_5.

Next, we investigated the formation of CF in the Ta_2O_5 channel by modulating the number (3, 6, 9, and 12) of neutral V_O along the z-axis and performing the geometry optimization of the channel region. Considering the system size, the 3, 6, 9, and 12 V_O corresponds to the V_O concentration conditions of 4.7×10^{19}, 9.3×10^{19}, 1.4×10^{20}, and 1.9×10^{20} cm^{-3}, respectively. We initially provided the V_O formation energy (ΔE) normalized by the number of V_O in the system (N_{V_O}) defined as,

$$\Delta E = {E_{V_O} - E_{pristine} + N_{V_O} \times (E_{O_2}/2)}\Big/{N_{V_O}}, \quad (4)$$

where $E_{pristine}$, E_{V_O}, and E_{O_2} are the ground-state energy of the Pt–Ta_2O_5–Pt junction without and with V_O [Pt–Ta_2O_{5-x}–Pt], and of a O_2 molecule in a vacuum, respectively. In Fig. 3(a), we show that the ΔE increases up to the 9 V_O case, and decreases slightly thereafter. Given that the ΔE corresponds

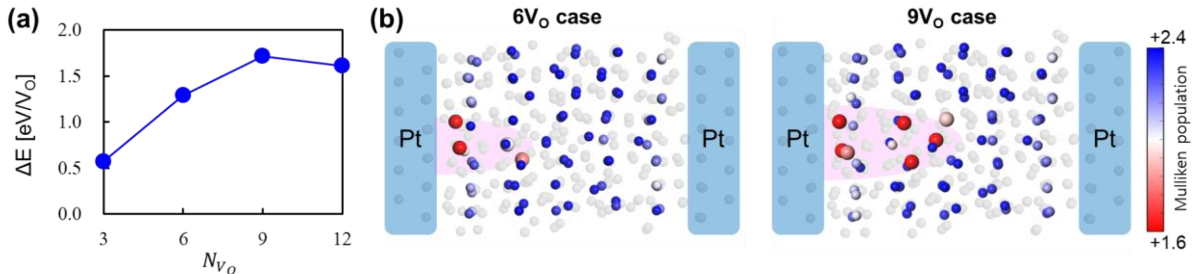

Fig. 3. (a) The formation energy of V_O with respect to the N_{V_O}. (b) Mulliken population analysis of Ta atoms in the cases of 6 V_O (*left*) and 9 V_O (*right*) models.

to the forming voltage qualitatively, it can be understood that the CF formation is controllable energetically until 9 V_O (1.4×10^{20} cm^{-3}) condition. Moreover, this finding implies that there exists the variation in the material properties of the tantala-based junction after 9 V_O, which will become clearer in the subsequent discussions of the electronic and transport properties of the Pt–Ta_2O_{5-x}–Pt junction.

Here, it should be reminded that the CF forming mechanism has been suggested as the redox reaction of Ta_2O_5/TaO_2 according to,

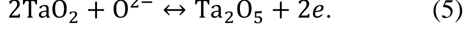

$$2\mathrm{TaO_2} + \mathrm{O}^{2-} \leftrightarrow \mathrm{Ta_2O_5} + 2e. \quad (5)$$

where the oxidation states of Ta of TaO_2 and Ta_2O_5 are Ta^{4+} and Ta^{5+}, respectively. Thus, we further presented the formation of the CF through visualizing the oxidation states of Ta atoms. The oxidation states of Ta atoms were determined by the partial charge of Ta atoms based on the Mulliken populations [Fig. 3(b)]. We show that the maximum charge displacement within Ta atoms is around 0.8 electrons, confirming that the two different Ta oxidation states are formed according to the V_O concentrations. Regardless of the degree of randomness of V_O distribution in our models, we found out that the clusters of TaO_{2-x} [red colored Ta atoms in Fig. 3(b)] were observed near the Pt(111)/Ta_2O_5 interface and grew with increasing the number of V_O. It can be understood that the relative instability of the Ta_2O_5 derived from the symmetry breaking of the Ta_2O_5 crystallinity at the interface can act as nucleation for initiating the CF forming process. In particular, the cluster of TaO_{2-x} can be achieved rather than its isolation due to the low V_O formation energy in Ta_2O_5 [Fig. 3(a)], which is in parallel with the previous report [15, 16].

Having confirmed the TaO_{2-x} CF formation under various V_O conditions, we investigated the transport properties of the cases with the 3, 6, 9, and 12 V_O. The *I*-V_b characteristics are provided in Fig. 4(a). The current value represents the current flowing through a single CF. We find out that the current level in both 9 and 12 V_O cases ($> \sim 1.4 \times 10^{20}\ cm^{-3}$) corresponds to the LRS with over 1000 times higher than the current of the HRS ($<$ 3 V_O, $\sim 5 \times 10^{19}\ cm^{-3}$) at V_b = 1.0 V.

To clarify the electronic origin of the HRS/LRS conduction mechanism, we provided spatially-resolved DOS and corresponding transmission spectra [Fig. 4(b)]. The changes in the ϕ_{SBH} and carrier concentration (n_e) on the tantala as function of the N_{V_O} are summarized in Fig. 4(c). In the case of the LRS, we clearly show that the ϕ_{SBH} decreases dramatically, which results in near Ohmic contact in the case of 9 and 12 V_O [Fig. 4(b) and (c)]. Besides, we confirmed that the n_e also increases with decreasing the ϕ_{SBH}. The corresponding transmission spectra confirm that the downshifted conduction band maximum [magenta solid lines in Fig. 4(b)] properly roles as a conducting channel states [leftward triangles in Fig. 4(b), *left*]. In parallel with the formation energy analysis [Fig. 3(a)], these findings indicate that the critical point of the TaO_{2-x} CF formation is $>\sim 1.4 \times 10^{20}\ cm^{-3}$ V_O conditions.

At this point, we note that unlike the resistive switching device performances based on conventional V_O-induced defect states-mediated conduction mechanism (*e.g.* trap-assisted tunneling) [17, 18], the performances based on the observed conduction mechanism in this study can be strongly affected by the band alignment at the Ta_2O_5-metal interfaces, which are in accord with the previous report [14]. Therefore, our work provides insight into the metal work function

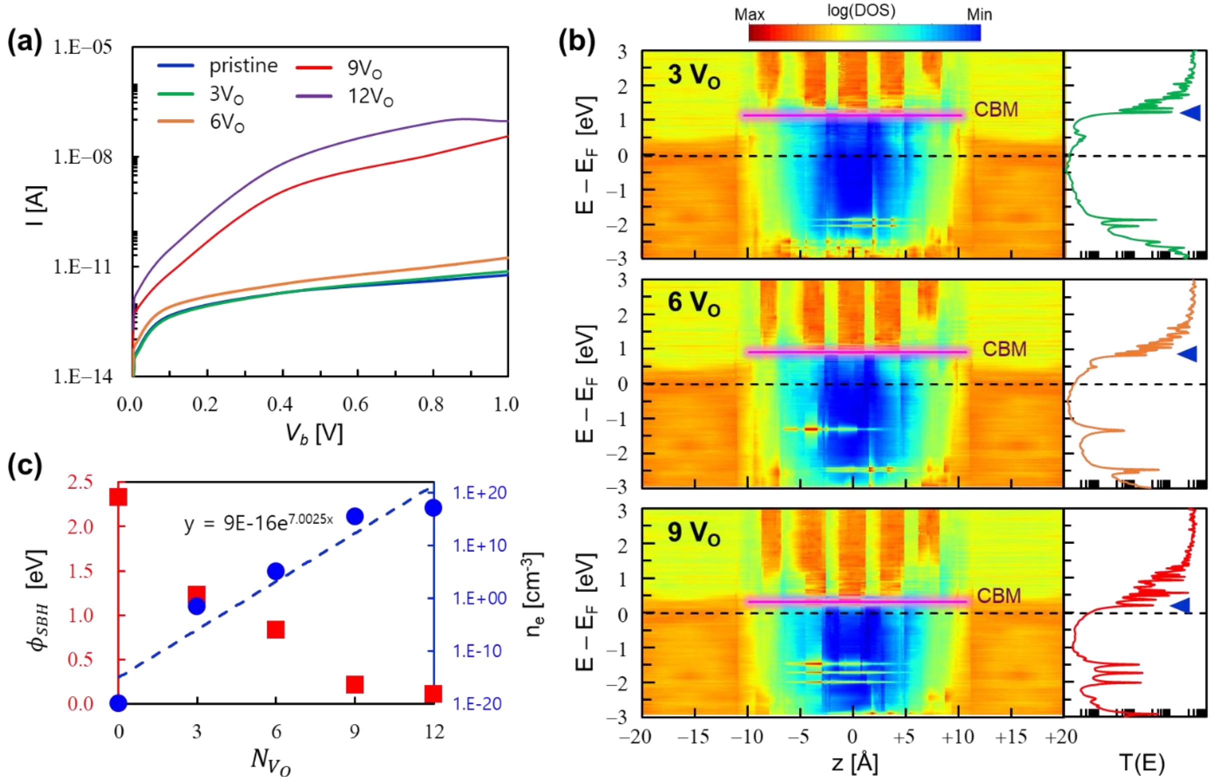

Fig. 4. (a) *I*-V_b characteristics according to the number of V_O conditions. (b) The corresponding spatially-resolved DOS (*left*) and transmission spectrum (*right*). (c) The summary of the $\boldsymbol{\phi_{SBH}}$ change with respect to the $\boldsymbol{N_{V_O}}$ and the corresponding n_e on the channel. Blue leftward triangles indicate the transmission peaks which originate from the tantala CBM.

engineering for the development of resistive switching devices.

IV. CONCLUSION

In summary, adopting a first-principles approach, we demonstrated the electrical and transport properties of the LRS/HRS of Pt/ Ta_2O_{5-x}/Pt heterojunctions. Focusing on the Ta_2O_5/TaO_2 redox reaction, we first observed the formation of the TaO_{2-x} CF according to the different number of V_O. Adopting the optimized structures with various TaO_{2-x} CF, we identified the I-V_b characteristics and revealed that the Ta_2O_5 matrix with over 9 V_O ($\sim 1.4 \times 10^{20}\ cm^{-3}$) assumes the LRS. Following electronic structure analyses, we finally identified that the HRS/LRS conduction mechanism in the tantala-based resistive devices originates from the n_e variation with the ϕ_{SBH} modulation according to the oxygen vacancy concentrations. Our findings yield insights for the design of next-generation resistive switching-based non-volatile memory devices.

REFERENCES

[1] H. Akinaga and H. Shima, “Resistive random access memory (ReRAM) based on metal oxides.” Proc. IEEE, vol. 98, pp. 2237-2251, 2010.

[2] C. Wang, H. Wu, B. Gao, T. Zhang, Y. Yang, and H. Qian, “Conduction mechanisms, dynamics and stability in ReRAMs”, Microelectron. Eng., vol. 187, pp. 121-133, 2018.

[3] Y. Chen, “ReRAM: History, status, and future”, IEEE Trans. Electron Devices, vol. 67, pp. 1420-1433, 2020.

[4] Z. Wei, et al. “Highly reliable TaOx ReRAM and direct evidence of redox reaction mechanism”, IEEE Int. Electron Dev. Meet., vol. 293, pp. 5671467, 2008.

[5] M.-J. Lee, C.B. Lee, D. Lee, S.R. Lee, M. Chang, J.H. Hur, Y.-B. Kim, C.-J. Kim, D.H. Seo, S. Seo, U-I. Chung, I.-K. Yoo, and K. Kim, “A fast, high-endurance and scalable non-volatile memory device made from asymmetric Ta_2O_{5-x}/TaO_{2-x} bilayer structures”, Nat. Mater., vol. 10, pp. 625-630, 2011.

[6] G.-S. Park, Y.B. Kim, S.Y. Park, X.S. Li, S. Heo, M.-J. Lee, M. Chang, J.H. Kwon, M. Kim, U-I. Chung, R. Dittmann, R. Waser, and K. Kim, “In situ observation of filamentary conducting channels in an asymmetric Ta_2O_{5-x}/TaO_{2-x} bilayer structure”, Nat. Commun., vol. 4, pp. 2382, 2013.

[7] S.-H. Lee, J. Kim, S.-J. Kim, S. Kim, and G.-S. Park, “Hidden structural order in orthorhombic Ta_2O_5”, Phys. Rev. Lett., vol. 110, pp. 235502, 2013.

[8] J.M. Soler, E. Artacho, J.D. Gale, A. Garcia, J. Junquera, P. Ordejon, and D. Sanchez-Portal, “The SIESTA method for ab initio order-N materials simulation”, J. Phys.: Condens. Matter, vol. 14, pp. 2745, 2002.

[9] J.P. Perdew, K. Burke, M. Ernzerhof, “Generalized gradient approximation made simple”, Phys. Rev. Lett., vol. 78, pp. 1396, 1997.

[10] J.-Y. Kim, B. Magyari-Kope, K.-J. Lee, H.-S. Kim, S.-H. Lee, and Y. Nishi, “Electronic structure and stability of low symmetry Ta_2O_5 polymorphs”, Phys. Status Solidi RRL, vol. 8, pp. 560-565, 2014.

[11] N. Truollier and J.L. Martins, “Efficient pseudopotentials for plane-wave calculations”, Phys. Rev. B Condens. Matter, vol. 43, pp. 1993-2006, 1991.

[12] M. Brandbyge, J.-L. Mozos, P. Ordejon, J. Taylor, and K. Stokbro, “Density-functional method for non-equilibrium electron transport”, Phys. Rev. B, vol. 65, pp. 165401, 2002.

[13] Datta, S. *Electronic Transport in Mesoscopic Systems* (Cambridge Univ. Press, 1995)

[14] V.Y.-Q. Zhuo, Y. Jiang, M.H. Li, E.K. Chua, Z. Zhang, J.S. Pan, R. Zhao, L.P. Shi, T.C. Chong, and J. Robertson, “Band alignment between Ta2O5 and metals for resistive random access memory electrode engineering”, Appl. Phys. Lett., vol. 102, pp. 062106, 2013.

[15] Y. Guo and J. Robertson, “Oxygen vacancy defects in Ta_2O_5 showing long-range atomic rearrangements”, Appl. Phys. Lett., vol. 104, pp. 112906, 2014.

[16] H. Jiang and D.A. Stewart, “Enhanced oxygen vacancy diffusion in Ta_2O_5 resistive memory devices due to infinitely adaptive crystal structure”, J. Appl. Phys., vol. 119, pp. 134502, 2016.

[17] A.L. Jagath, T.N. Kumar, and H.A.F. Almurib, “Modeling of current conduction during RESET phase of Pt/Ta2O5/TaOx/Pt bipolar resistive RAM devices”, 2018 IEEE NVMSA, pp. 55-60, 2018.

[18] W. Goes, D. Green, P. Blaise, G. Piccolboni, A. Bricalli, A. Regev, G. Molas, J.-F. Nodin, “A comprehensive oxide-based ReRAM TCAD model with experimental verification”, 2021 IEEE IMW, pp. 1-4, 2021.